Ultrathin Gold Nanowire-Functionalized Carbon Nanotubes for Hybrid Molecular Sensing

Huizhong Cui,[†] Chenglin Hong,[†,§] Andrew Ying,[†] Xinmai Yang,[‡] and Shenqiang Ren[†,*]

[†]Department of Chemistry, University of Kansas, Lawrence, Kansas, 66045, United States, [‡]Bioengineering Research Center, Department of Mechanical Engineering, University of Kansas, Lawrence, Kansas 66045, United States, and [§]College of Chemistry and Chemical Engineering, Shihezi University, Shihezi 832003, China

ABSTRACT Carbon nanotubes (CNTs) have shown great potential as sensing component in the electrochemical field effect transistor and optical sensors, because of their extraordinary one-dimensional electronic structure, thermal conductivity, and tunable and stable near-infrared emission. However, the insolubility of CNTs due to strong van der Waals interactions limits their use in the field of nanotechnology. In this study, we demonstrate that noncovalent ultrathin gold nanowires functionalized multiwalled carbon nanotube (GNW-CNT) hybrid sensing agents show highly efficient and selective immune molecular sensing in electrochemical and near-infrared photoacoustic imaging methods. A detection limit of 0.01 ng/mL for the alpha-fetoprotein (AFP) antigen with high selectivity is shown. The extraordinary optical absorption, thermal, and electric conductivity of hybrid GNW-CNTs presented in this study could be an effective tactic to integrate imaging, sensing, and treatment functionalities.

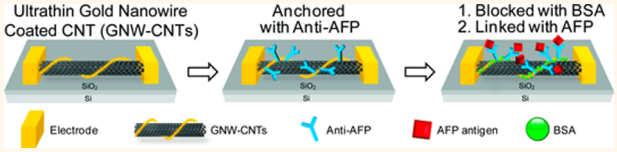

KEYWORDS: carbon nanotubes · gold nanowires · *in situ* synthesis · electrochemical · photoacoustic imaging

Carbon nanotubes (CNTs) classified as single-walled CNTs (SWCNTs) and multiwalled CNTs (MWCNTs) have been attracting much interest since they were first introduced in the 1990s, because of their excellent chemical stability, high thermal and electronic conductivity, and broad spectral optical absorption. Therefore, CNTs have been intensively investigated in many emerging applications, including field-effect emitters,[1,2] solar cells,[3−5] and hydrogen storage medium.[6−8]

In recent years, CNTs have shown great potential in biomedical applications, such as bioimaging, sensing and drug delivery in cells and animals due to their strong optical absorption, high thermal conductivity and long-circulating characteristics.[9−13] Particularly, CNTs absorb light in the near-infrared (NIR, such as 700−900 nm), where tissue optical scattering and absorption reaches minima; thus, they can image more deeply within tissues with high spatial resolution. CNTs have been used in various biomedical imaging applications, such as NIR photoluminescence imaging,[14] Raman imaging,[15,16] magnetic resonance imaging (MRI),[17,18] and photoacoustic (PA) imaging.[19−24] However, due to their highly hydrophobic property, surface functionalization of CNTs should be performed to obtain high water solubility and biocompatibility before bioconjugation process. In the past, the chemical covalent or physical noncovalent approaches have been employed for surface functionalization.[25−29] Chemical reactions are most widely studied to covalently functionalize CNTs by using harsh experimental conditions, such as strong acids or oxidants, but they usually create a number of defects on the sidewalls of CNTs that affect their electronic and optical properties.[30] Noncovalent interactions utilize the surfactant or polymers to coat on CNTs, which show promise to increase their water solubility, prevent the aggregation and enhance their biocompatibility.[31] However, noncovalent interactions between CNTs and surfactant or polymers are not stable in the biological fluids, and simultaneously preserving the optical property of the CNTs remains as a central challenge.

In this study, we develop *in situ* solution-phase synthesis of ultrathin gold nanowires (GNWs) incorporated MWCNTs as a model sensing system, in which noncovalent

* Address correspondence to shenqiang@ku.edu.

Received for review May 30, 2013 and accepted August 29, 2013.

Published online August 29, 2013
10.1021/nn4027323

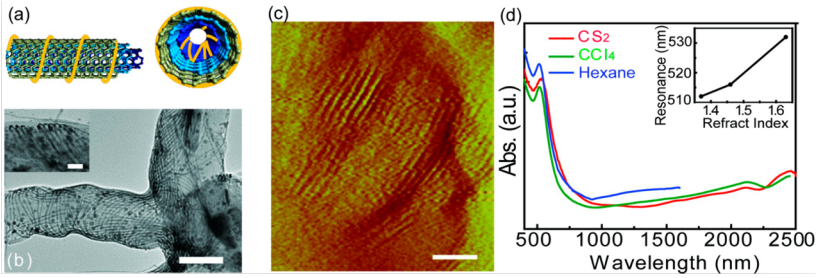

Figure 1. (a) Schematic of GNW-CNTs. (b) TEM image, scale bars: 50 nm. Inset scale bar: 20 nm. (c) AFM image, scale bars: 100 nm. (d) Absorption spectra of GNW-CNTs. The inset shows the red-shift in the LSPR maximum with increasing solvent refractive index.

functionalization is shown to provide efficient electrochemical sensing and NIR PA imaging. The ultrahigh surface to volume ratio of the MWCNTs and *in situ* GNWs synthesis allows for efficient inside and outside noncovalent functionalization. Since ultrathin gold nanowire surfaces exhibit excellent biocompatibility to incorporate additional surface functionalities,[32,33] the resulting water-soluble hybrids exhibit high optical absorbance while obtaining the abilities of bioconjugation, and also extraordinary thermal conductivity than that of MWCNTs, which is an important property for PA imaging. Additionally, we show the hybrid GNW-CNTs can be selective for detecting alpha-fetoprotein (AFP) antigen as the model system, using both electrochemical and NIR PA imaging techniques. AFP antigen is the early indicator of hepatocarcinogenesis and an important biomarker of hepatocellular carcinoma (HCC), which is the most common type of liver cancer.[34−36] Our results demonstrate that the GNW-CNT hybrids can offer a promising alternative for noninvasive detection of AFP antigen.

In the following report, the structure of solution-phase GNW-CNTs will be first introduced. Moreover, we will show the PA imaging characteristics based on unique optical and thermal properties of the hybrid system. The GNW-CNTs hybrids for sensing the AFP antigen using both electrochemistry and PA imaging will also be presented.

RESULTS AND DISCUSSION

Figure 1a shows the schematic structure of the GNW-CNT hybrids. The GNW-CNTs consist of a multiwalled carbon nanotube core with a diameter of 40−60 nm, which is noncovalently incorporated with ultrathin gold nanowires. To enhance water solubility of GNW-CNT, cetyltrimethylammonium bromide (CTAB) and sodium citrate were used to transfer GNW-CNT hybrid phase from hexane to water. The well dispersed GNW-CNTs with relatively uniform size were highly water-soluble due to gold nanowire surface functionalization. Transmission electron microscopy (TEM) analysis of the GNW-CNTs (Figure 1b) demonstrates that the gold nanowires with a diameter about 1 nm are incorporated outside and inside MWCNTs. Surface

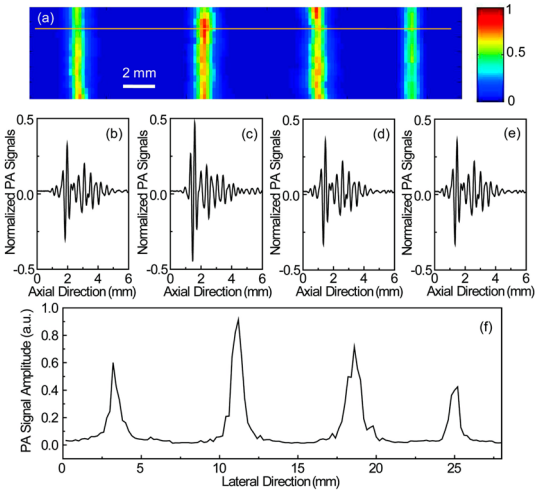

Figure 2. (a) PA MAP image of four particle solutions in tubings (from left to right: plain MWCNTs, MWCNTs wrapped with GNWs, MWCNTs mixed with GNWs, and pure GNWs); (b−e) PA signals from particle solutions; (f) signal profile at the horizontal dashed line position in (a).

morphology of hybrid GNW-CNTs thin films by atomic force microscopy (AFM) confirms the fiber-like structure, shown in Figure 1c. The photoabsorption spectra of the GNW-CNTs (Figure 1d) show a transverse plasmon absorption in the visible region (510−530 nm) and a wide longitudinal resonance peak in the IR region. Compared to the absorption spectrum of MWCNTs (Supplementary Figure 2), we attribute the IR absorption to a high aspect ratio of ultrathin gold nanowires.[37] To confirm this localized surface plasmon resonance (LSPR), we study the refractive index effect of the solvent medium on the photoabsorption of GNW-CNT hybrids. Three different solvents have been applied: hexane, carbon tetrachloride (CCl_4), and carbon sulfide (CS_2) with refractive indices of 1.37, 1.46, and 1.63, respectively. The inset of Figure 1d indicates that the absorption band from GNW-CNTs red-shifts with increasing refractive index, which confirms the LSPR feature of ultrathin gold nanowires incorporated CNTs, but not scattering or sample impurities.[38] The absorption of GNW-CNTs in hexane over 1600 nm incident light wavelength was not included in the figure, because the hexane shows extremely high

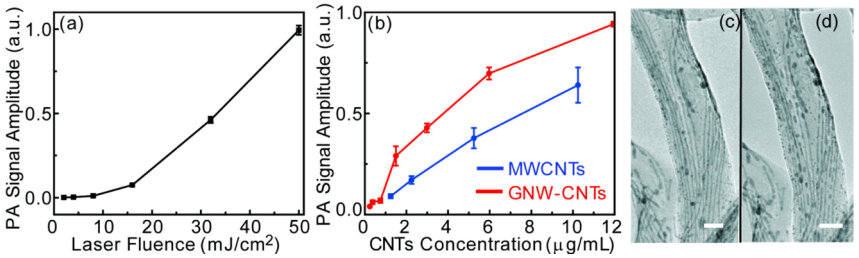

Figure 3. (a) PA signal amplitudes from GNW-CNTs as a function of laser fluence; (b) PA signals amplitudes as a function of CNTs concentration. The error bars represent the standard deviation in five measurements; blue line, PA amplitude from MWCNTs; red line, PA amplitude from GNW-CNTs. (c and d) TEM images showing gold nanowires degradation upon long exposure to the high-energy electron beam during HRTEM analysis; scale bars, 20 nm.

intensity noise and strong interference in the signals from GNW-CNTs.

For PA applications, we explore the PA signal amplitudes of MWCNTs, GNW-CNT hybrids, MWCNTs mixed with GNWs, and GNWs, shown in Figure 2. Figure 2a shows corresponding maximum amplitude projection (MAP) PA images. Figure 2b−e show the PA signals and the signal profile at the horizontal dashed line position in (a), respectively. The GNW-CNT hybrids exhibit significantly stronger PA signal amplitudes than those of MWCNTs and GNWs. Since the PA imaging is an absorption-based technique, the enhancement in PA amplitude is a result of the increase in optical absorption of GNW-CNT hybrids. Particularly, the PA amplitude of GNW-CNTs was also stronger than that of the randomly mixed GNWs and MWCNTs. The enhancement of GNW-CNT over CNT mixed with GNW was calculated to be about 25.66%. We attribute such PA signal amplitude increase to the enhanced absorption from NIR plasmonic resonance of GNWs under 820 nm laser wavelength used in the PA imaging. Therefore, GNW-CNTs exhibit higher optical absorption than that of MWCNT, leading to strong PA signals. In addition, the GNWs are wrapped and incorporated into MWCNTs to facilitate the formation of percolation network and the interaction between GNW and MWCNT, which will enhance thermal transfer and the overall thermal conductivity of the hybrids structure.

In addition, the PA signal amplitude is dependent on the applied laser fluence and the MWCNT concentration. Figure 3a shows a nonlinear signal enhancement as the laser fluence increases at 820 nm laser wavelength. We postulate that the nonlinear PA signal increase is originated from the change of thermal expansion coefficient at the high laser fluence during the local temperature increase with thermal coupling.[39−41] It is consistent with previous reports that the PA amplitude of MWCNTs exhibits a linear relationship as their concentration increases (Figure 3b). However, the amplitude from the GNW-CNT hybrids shows a drastic enhancement starting from ~1.5 μg/mL CNTs concentration compared to that of MWCNTs. This result further confirms that the integrated structure of GNWs and MWCNTs can result in enhanced optical

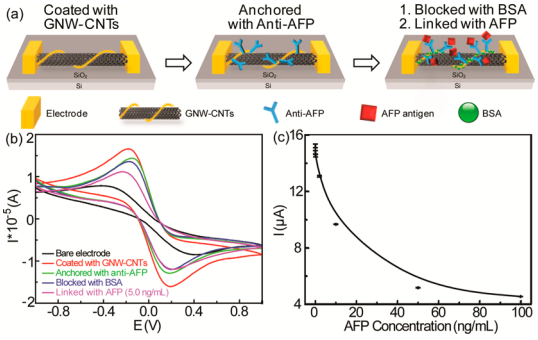

Figure 4. (a) Schematic image of the bioconjugation for the electrochemistry immune test; (b) peak current amplitude in different steps of modified electrodes; (c) peak current as a function of the AFP antigen concentration.

absorption and improved thermal properties and, thus, stronger PA signal amplitude. The morphological change of GNWs under long laser exposure was also observed. TEM images (Figure 3c,d) show the melting behavior of GNWs on MWCNTs before and after high intensity laser energy, in which the GNWs were disconnected into rods slowly and into spheres eventually over time. A similar process has been reported for the gold nanowires under HRTEM analysis.[42] In addition, we found that the GNW-CNTs melted faster than those free GNWs which were not attached on the MWCNTs (see Supplementary Figure 3), which could be attributed to the high thermal conductivity of CNTs to transfer heat to the GNWs causing the melting behavior. This characteristic may have the potential as cancer drug carrier for the drug release into the targeting area under the laser irradiation for future drug delivery and cancer treatment.[43]

For specific molecular sensing and targeting applications, we explore the GNW-CNT hybrids by functionalizing GNWs with the antibody, which is specific to the AFP antigen. Figure 4a shows the schematic of each step for the immune test using the electrochemistry method. In this test, GNWs on the surface of MWCNT can facilitate the Au−S interaction with the thiol groups of Cys residues in anti-AFP,[44] which enhances the affinity of anti-AFP to GNW-CNT. Figure 4b shows the redox peak current under different testing conditions. The redox peak current of the GNW-CNT

modified electrode is significantly higher than that of bare electrodes without GNW-CNTs, suggesting that the GNW-CNTs film enhances electron transfer by providing a more conductive medium for the electron movement. After the electrode was coated with anti-AFP antibody and bovine serum albumin (BSA) films, the peak currents of the electrode decreased significantly as a result of the low conductivity of anti-AFP/BSA films. In addition, the incubation of electrode with AFP antigen caused the peak current to decrease even more. Figure 4c shows that the peak current has a nonlinear decrease as AFP antigen concentration increases. The presented results were obtained from repeated experiments, and a small data spread range from the error bar showed an excellent reproducibility of this electrochemical sensing. As AFP concentration increases, the signal change to concentration ratio is decreased. This result can be understood by the consideration of the molecular size. As the concentration of AFP antigen increases, the incoming molecules were sterically hindered by the existed bioconjugated antigen. The result from the immune test using electrochemistry confirms the capability of GNW-CNTs for simple and robust bioconjugation. On the basis of the traditional protocol, the limit of detection (LOD) is estimated to the concentration corresponding to three times of the standard deviation of the noise. The standard deviation from our repeated experiments without AFP was shown to be 0.13 μA. The difference of signal amplitude with AFP at a concentration of 0.01 ng/mL, and without AFP, is about 0.87 μA. It should be noted that 0.01 ng/mL AFP can be detected with this sensor by considering the standard deviation (0.39 μA) lower than 0.87 μA.

To further investigate the feasibility of GNW-CNTs to detect AFP antigen, PA imaging immune test was conducted. Figure 5a shows a similar bioconjugation process for the PA imaging immune test. The biotinylated monoclonal antibody (BMA), which attached on the bottom of the microplates, was not well dispersed but accumulated on the corner as shown in Figure 5b. The PA imaging was performed on both treated wells and controlled wells. In Figure 5c,d, the weak PA signal amplitudes can be observed from the controlled wells. In the PA images of treated wells (Figure 5e−h, the bright area, showing the enhancement in the PA signals, indicates the existence of the GNW-CNTs and demonstrates that AFP antigen coupling to anti-AFP antibody conjugated GNW-CNTs can be monitored by the increase in the PA signal amplitude. In addition, the bright area matches very well with the location of the BMA. To quantify the change of PA amplitude after linking anti-AFP antibody conjugated GNW-CNTs with different concentrations of AFP, we calculated averaged PA amplitude enhancement in the approximate BMA immobilized region (Figure 5b). Figure 5I shows the calculated PA amplitude as a function of AFP

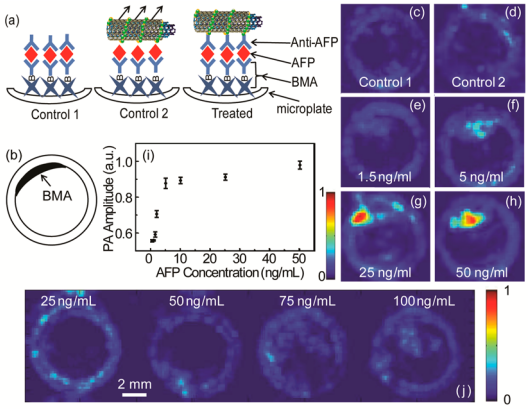

Figure 5. (a) Schematic image of the controlled and treated methods of immune tests using GNW-CNTs; (b) scheme showing the location of the Biotinylated Monoclonal Antibody (BMA) on the bottom of microplates; (c and d) PA images on controlled microplates; (e−h) PA images from treated microplates with different AFP concentrations as labeled; (i) PA signals amplitudes from GNW-CNTs as a function of AFP antigen concentration; (j) PA images from treated microplates with different AFP concentrations as labeled, using GNWs as sensor.

antigen concentration. The PA amplitude shows a linear enhancement until 5 ng/mL AFP antigen concentration, below which the antibody functionalized GNW-CNTs were gradually immobilized on the increasing number of AFP antigen, leading to the increased PA signal amplitude. However, when AFP antigen concentration is higher than 5 ng/mL, the PA amplitude reaches a saturation level, which agrees with the result from electrochemistry method, and can be attributed by the sterically hindering of large molecular size AFP antigen.

To demonstrate that GNW-CNT hybrids have better sensing sensitivity than GNW, the immune test using GNW as the sensor was performed. First, anti-AFP was immobilized on the surface of GNWs by mixing two solutions for 12 h. Second, bovine serum albumin (BSA) was added to the resulting solution for blocking nonspecific absorber site on the GNWs for another 2 h. Third, 25 μL of AFP serum was pipetted into the assigned biotinylated monoclonal antibody (BMA) coated microwells with different concentrations for incubating at room temperature and the mixture was washed with PBS solution after 20 min in order to link the antibody to BMA. BMA was higher dose than AFP. Finally, 100 μL of the anti-AFP antibody conjugated GNWs was added to each well and the mixture was washed again with PBS solution after 20 min. The PA images were obtained on the treated microwells with different AFP concentrations as shown in figure 1. From the images, we can observe very weak PA signals from the center of the microwells at 25 and 50 ng/mL AFP concentrations. At 75 and 100 ng/mL AFP concentrations, PA signals become stronger because of the attachment of more GNWs on the microwells. However, we can observe very strong PA signals at 5 ng/mL

AFP concentration with GNW-CNT as the sensor. Therefore, it is concluded that GNW-CNT hybrids have a much better sensitivity than GNWs.

CONCLUSIONS

In summary, we demonstrate solution-phase synthesized ultrathin gold nanowires incorporated carbon nanotube hybrids as both NIR photoacoustic imaging and efficient electrochemical sensing agents. Noncovalent ultrathin gold nanowire functionalized CNTs preserve the extraordinary optical and thermal properties, and more importantly, exhibit high water solubility and further biological molecule functionalization. The presented hybrid golden carbon nanotubes own high optical absorption, thermal and electric conductivity. We showed the high selectivity and sensing efficiency of hybrid GNW-CNTs by conjugating with targeted molecules. In addition, the morphology change under laser exposure and high thermal conductivity of CNTs also facilitates the disconnection process of GNWs, which could open up potential applications by releasing the drug conjugated on the GNWs into the targeted area under the laser illumination at certain intensity. Moreover, we showed that GNW-CNT conjugated with anti-AFP antigen has the ability to specifically link to the AFP antigen, and demonstrated a detection limit of 0.01 ng/mL for the AFP antigen with high selectivity, as one model detection system.

EXPERIMENTAL METHODS

***In Situ* Synthesis of Ultrathin GNW-CNTs.** In a typical synthesis, MWCNTs were dispersed in hexane with 0.5 mg/mL concentration. Then, 100 μL of oleylamine (OA) mixed with 3 mg of $HAuCl_4$ was added to the 2.5 mL of MWCNTs and hexane mixture, followed by the addition of 150 μL of triisopropylsilane (TIPS) to form a solution. Then the reaction proceeded at room temperature without stirring for 24 h. The final products were centrifuged, washed with ethanol and finally redispersed in hexane for further investigation.

To enhance water solubility of GNW-CNT, the following modification process has been performed. A mixture of 0.1 M cetyltrimethylammonium bromide (CTAB) and 0.01 mM sodium citrate was added to GNW-CNT solution for phase transfer from hexane to water. The transfer will be completed after at least 24 h. GNW-CNT in water was used for immune test.

PA Imaging System Setup. The system schematic is shown in Supplementary Figure 5. The system consists of an ultrasound transducer, a laser system, and receiving electronics. A Q-switched Nd:YAG laser (Surelite; Continuum, Santa Clara, CA) was used to pump a tunable OPO laser (Surelite OPO PLUS; Continuum, Santa Clara, CA) to obtain a 820 nm wavelength laser with a 10-Hz pulse repetition rate. The produced laser light forms a ring shape illumination after passing through several prisms and a conical lens and then is refocused inside the sample by an optical condenser. The subsequently generated ultrasonic waves are detected by a 5-MHz focused ultrasonic transducer (SU-108-013; Sonic Concepts, Bothell, WA) which was mounted in the middle of the condenser lens. The conical and condenser lenses were driven by a 3D translation stage to enable the transducer to mechanically scan the targeted region. Two prisms were used to enable the optical beam-folding for a 2D mechanical scanning. Prism Y could only move on the *Y* direction, whereas prism XY could move on both *X* and *Y* direction. The recorded photoacoustic signals by the transducer were amplified through a preamplifier (5072PR; Olympus-NDT, Waltham, MA) and then collected by a PC through an A/D Scope Card (CS21G8−256MS; Gage, Lockport, IL) with a 250-MHz sampling rate. This design was presented by Song *et al.*[45] for the deep PAI, and proved to generate high-resolution photoacoustic images in deep regions inside the soft tissue.[46]

PA Signals Amplitude Comparison among Four Nanoparticles. Four different particle solutions dispersed in DI water were injected into the tygon tubing with GNWs and MWCNTs concentrations of 0.35 and 0.5 mg/mL for PA imaging. Laser wavelength and laser fluence used in this experiment was 820 nm and 14 mJ/cm^2, respectively.

Electrochemistry Immune Test. In electrochemistry assessment of the functionalization capability of GNW-CNTs, The patterned gold electrode was sputtered with 100 nm thickness using Sputter Coater on a Si substrate. First, 40 μL of GNW-CNTs were spin-coated on the cleaned electrode at 1800 rpm for 30 s and the electrode was washed with DI water. Second, 30 μL of anti-AFP antibody solution was dropped on the electrode for 12 h at 4 °C to anchor the antibody on the surface of the electrode. Third, 40 μL of bovine serum albumin (BSA) solution was dipped on the electrode for about 2 h at 4 °C in order to block possible remaining nonspecific binding of GNW-CNTs active sites. At last, 30 μL of AFP serum at different concentrations was dipped on the electrodes for linking with the anti-AFP antibody for about 20 min. The obtained electrode was then washed carefully with DI water and stored at 4 °C before using. The schematic of the bioconjugation process is shown in Figure 4a. Cyclic voltammograms of the different steps of modified electrodes were then carried out in pH 7.5 PBS buffer containing 1.0 mmol/L $Fe(CN)_6^{3-/4-}$ (Figure 4b).

Photoacoustic Immune Test. AFP antibody was immobilized on the surface of GNW-CNTs by mixing two solutions for 12 h. Then, BSA was added to the resulting solution for blocking nonspecific absorber site on the GNW-CNTs for another 2 h. The anti-AFP antibody conjugated GNW-CNTs were ready to use. For the treated group, 25 μL of AFP serum was pipetted into the assigned BMA coated microwells with different concentrations for incubating at room temperature and the mixture was washed with PBS solution after 20 min in order to link the antibody to BMA. BMA were higher dosed than AFP. Then, 100 μL of the anti-AFP antibody conjugated GNW-CNTs was added to each well and the mixture was washed again with PBS solution after 20 min. For controlled group 1, only anti-AFP antibody is added to the AFP-incubated well. For controlled group 2, bare GNW-CNTs, which were not conjugated with anti-AFP antibody but blocked by BSA, were added to the AFP-incubated well. The laser wavelength and fluence used in the immune test was 820 nm and 14 mJ/cm^2, respectively.

Conflict of Interest: The authors declare no competing financial interest.

Acknowledgment. S.R. acknowledges funding from the National Institute of General Medical Sciences of the National Institutes of Health under Award Number P20GM103638. The content is solely the responsibility of the authors and does not necessarily represent the official views of the National Institutes of Health. C.H. acknowledges scholarship from China Scholarship Council.

Supporting Information Available: Description of particle synthesis, photoacoustic imaging instrument, morphology change of GNWs, experimental procedures. This material is available free of charge *via* the Internet at http://pubs.acs.org.

REFERENCES AND NOTES

1. Niemann, D. L.; Ribaya, B. P.; Gunther, N.; Rahman, M.; Leung, J.; Nguyen, C. V. Effects of Cathode Structure on the

Field Emission Properties of Individual Multi-Walled Carbon Nanotube Emitters. *Nanotechnology* **2007**, *18*, 485702.
2. Park, N.; Han, S. W.; Ihm, J. Effects of Oxygen Adsorption on Carbon Nanotube Field Emitters. *Phys. Rev. B* **2001**, *64*, 125401.
3. Kongkanand, A.; Dominguez, R. M.; Kamat, P. V. Single Wall Carbon Nanotube Scaffolds for Photoelectrochemical Solar Cells. Capture and Transport of Photogenerated Electrons. *Nano Lett.* **2007**, *7*, 676–680.
4. Lu, R.; Christianson, C.; Kirkeminde, A.; Ren, S.; Wu, J. Extraordinary Photocurrent Harvesting at Type-II Heterojunction Interfaces: Toward High Detectivity Carbon Nanotube Infrared Detectors. *Nano Lett.* **2012**, *12*, 6244–6249.
5. Ruzicka, B. A.; Wang, R.; Lohrman, J.; Ren, S.; Zhao, H. Exciton Diffusion in Semiconducting Single-Walled Carbon Nanotubes Studied by Transient Absorption Microscopy. *Phys. Rev. B* **2012**, *86*, 205417.
6. Dillon, A. C.; Jones, K. M.; Bekkedahl, T. A.; Kiang, C. H.; Bethune, D. S.; Heben, M. J. Storage of Hydrogen in Single-Walled Carbon Nanotubes. *Nature* **1997**, *386*, 377–379.
7. Lee, S. M.; Lee, Y. H. Hydrogen Storage in Single-Walled Carbon Nanotubes. *Appl. Phys. Lett.* **2000**, *76*, 2877–2879.
8. Liu, C.; Fan, Y. Y.; Liu, M.; Cong, H. T.; Cheng, H. M.; Dresselhaus, M. S. Hydrogen Storage in Single-Walled Carbon Nanotubes at Room Temperature. *Science* **1999**, *286*, 1127–1129.
9. de la Zerda, A.; Liu, Z.; Bodapati, S.; Teed, R.; Vaithilingam, S.; Khuri-Yakub, B. T.; Chen, X.; Dai, H.; Gambhir, S. S. Ultrahigh Sensitivity Carbon Nanotube Agents for Photoacoustic Molecular Imaging in Living Mice. *Nano Lett.* **2010**, *10*, 2168–2172.
10. De La Zerda, A.; Zavaleta, C.; Keren, S.; Vaithilingam, S.; Bodapati, S.; Liu, Z.; Levi, J.; Smith, B. R.; Ma, T.-J.; Oralkan, O.; *et al.* Carbon Nanotubes as Photoacoustic Molecular Imaging Agents in Living Mice. *Nat. Nanotechnol.* **2008**, *3*, 557–562.
11. Pramanik, M.; Song, K. H.; Swierczewska, M.; Green, D.; Sitharaman, B.; Wang, L. V. *In Vivo* Carbon Nanotube-Enhanced Non-Invasive Photoacoustic Mapping of the Sentinel Lymph Node. *Phys. Med. Biol.* **2009**, *54*, 3291–3301.
12. Pramanik, M.; Swierczewska, M.; Green, D.; Sitharaman, B.; Wang, L. V. Single-Walled Carbon Nanotubes as a Multimodal-Thermoacoustic and Photoacoustic-Contrast Agent. *J. Biomed. Opt.* **2009**, *14*, 034018.
13. Xiang, L.; Yuan, Y.; Xing, D.; Ou, Z.; Yang, S.; Zhou F. Photoacoustic Molecular Imaging with Antibody-Functionalized Single-Walled Carbon Nanotubes for Early Diagnosis of Tumor. *J. Biomed. Opt.* **2009**, *14*, 021008.
14. Lefebvre, J.; Austing, D. G.; Bond, J.; Finnie, P. Photoluminescence Imaging of Suspended Single-Walled Carbon Nanotubes. *Nano Lett.* **2006**, *6*, 1603–1608.
15. Doorn, S. K.; Zheng, L. X.; O'Connell, M. J.; Zhu, Y. T.; Huang, S. M.; Liu, J. Raman Spectroscopy and Imaging of Ultralong Carbon Nanotubes. *J. Phys. Chem. B* **2005**, *109*, 3751–3758.
16. Mews, A.; Koberling, F.; Basche, T.; Philipp, G.; Duesberg, G. S.; Roth, S.; Burghard, M. Raman Imaging of Single Carbon Nanotubes. *Adv. Mater. (Weinheim, Ger.)* **2000**, *12*, 1210–1214.
17. Al Faraj, A.; Cieslar, K.; Lacroix, G.; Gaillard, S.; Canot-Soulas, E.; Cremillieux, Y. *In Vivo* Imaging of Carbon Nanotube Biodistribution Using Magnetic Resonance Imaging. *Nano Lett.* **2009**, *9*, 1023–1027.
18. Wu, H.; Liu, G.; Wang, X.; Zhang, J.; Chen, Y.; Shi, J.; Yang, H.; Hu, H.; Yang, S. Solvothermal Synthesis of Cobalt Ferrite Nanoparticles Loaded on Multiwalled Carbon Nanotubes for Magnetic Resonance Imaging and Drug Delivery. *Acta Biomater.* **2011**, *7*, 3496–3504.
19. Xu, M. H.; Wang, L. H. V. Photoacoustic Imaging in Biomedicine. *Rev. Sci. Instrum.* **2006**, *77*, 041101.
20. Esenaliev, R. O.; Karabutov, A. A.; Oraevsky, A. A. Sensitivity of Laser Opto-Acoustic Imaging in Detection of Small Deeply Embedded Tumors. *IEEE J. Sel. Top. Quantum Electron.* **1999**, *5*, 981–988.
21. Hoelen, C. G. A.; de Mul, F. F. M.; Pongers, R.; Dekker, A. Three-Dimensional Photoacoustic Imaging of Blood Vessels in Tissue. *Opt. Lett.* **1998**, *23*, 648–650.
22. Wang, L. V. Tutorial on Photoacoustic Microscopy and Computed Tomography. *IEEE J. Sel. Top. Quantum Electron.* **2008**, *14*, 171–179.
23. Ku, G.; Wang, L. H. V. Deeply Penetrating Photoacoustic Tomography in Biological Tissues Enhanced with an Optical Contrast Agent. *Opt. Lett.* **2005**, *30*, 507–509.
24. Song, K. H.; Wang, L. V. Deep Reflection-Mode Photoacoustic Imaging of Biological Tissue. *J. Biomed. Opt.* **2007**, *12*, 060503.
25. Liu, J. Q.; Chou, A.; Rahmat, W.; Paddon-Row, M. N.; Gooding, J. J. Achieving Direct Electrical Connection to Glucose Oxidase Using Aligned Single Walled Carbon Nanotube Arrays. *Electroanalysis* **2005**, *17*, 38–46.
26. Gooding, J. J.; Wibowo, R.; Liu, J. Q.; Yang, W. R.; Losic, D.; Orbons, S.; Mearns, F. J.; Shapter, J. G.; Hibbert, D. B. Protein Electrochemistry Using Aligned Carbon Nanotube Arrays. *J. Am. Chem. Soc.* **2003**, *125*, 9006–9007.
27. Kim, J.; Baek, J.; Kim, H.; Lee, K.; Lee, S. Integration of Enzyme Immobilized Single-Walled Carbon Nanotubes Mass into the Microfluidic Platform and Its Application for the Glucose-Detection. *Sens. Actuators, A* **2006**, *128*, 7–13.
28. Wang, H.; Wang, C. C.; Lei, C. X.; Wu, Z. Y.; Shen, G. L.; Yu, R. Q. A Novel Biosensing Interfacial Design Produced by Assembling Nano-Au Particles on Amine-Terminated Plasma-Polymerized Films. *Anal. Bioanal. Chem.* **2003**, *377*, 632–638.
29. Wang, Y.; Joshi, P. P.; Hobbs, K. L.; Johnson, M. B.; Schmidtke, D. W. Nanostructured Biosensors Built by Layer-by-Layer Electrostatic Assembly of Enzyme-Coated Single-Walled Carbon Nanotubes and Redox Polymers. *Langmuir* **2006**, *22*, 9776–9783.
30. Sui, X.-M.; Giordani, S.; Prato, M.; Wagner, H. D. Effect of Carbon Nanotube Surface Modification on Dispersion and Structural Properties of Electrospun Fibers. *Appl. Phys. Lett.* **2009**, *95*, 233113.
31. Shi, J.; Cha, T.-G.; Claussen, J. C.; Diggs, A. R.; Choi, J. H.; Porterfield, D. M. Microbiosensors Based on DNA Modified Single-Walled Carbon Nanotube and Pt Black Nanocomposites. *Analyst* **2011**, *136*, 4916–4924.
32. Mukhopadhyay, K.; Phadtare, S.; Vinod, V. P.; Kumar, A.; Rao, M.; Chaudhari, R. V.; Sastry, M. Gold Nanoparticles Assembled on Amine-Functionalized Na-Y Zeolite: A Biocompatible Surface for Enzyme Immobilization. *Langmuir* **2003**, *19*, 3858–3863.
33. Eustis, S.; El-Sayed, M. A. Why Gold Nanoparticles Are More Precious Than Pretty Gold: Noble Metal Surface Plasmon Resonance and Its Enhancement of the Radiative and Nonradiative Properties of Nanocrystals of Different Shapes. *Chem. Soc. Rev.* **2006**, *35*, 209–217.
34. Johnson, P. J. The Role of Serum Alpha-Fetoprotein Estimation in the Diagnosis and Management of Hepatocellular Carcinoma. *Clin. Liver Dis.* **2001**, *5*, 145–159.
35. Trevisani, F.; D'Intino, P. E.; Morselli-Labate, A. M.; Mazzella, G.; Accogli, E.; Caraceni, P.; Domenicali, M.; De Notariis, S.; Roda, E.; Bernardi, M. Serum Alpha-Fetoprotein for Diagnosis of Hepatocellular Carcinoma in Patients with Chronic Liver Disease: Influence of Hbsag and Anti-Hcv Status. *J. Hepatol.* **2001**, *34*, 570–575.
36. Yamashita, T.; Forgues, M.; Wang, W.; Kim, J. W.; Ye, Q.; Jia, H.; Budhu, A.; Zanetti, K. A.; Chen, Y.; Qin, L.-X.; *et al.* Epcam and Alpha-Fetoprotein Expression Defines Novel Prognostic Subtypes of Hepatocellular Carcinoma. *Cancer Res.* **2008**, *68*, 1451–1461.
37. Guidez, E. B.; Aikens, C. M. Theoretical Analysis of the Optical Excitation Spectra of Silver and Gold Nanowires. *Nanoscale* **2012**, *4*, 4190–4198.
38. Luther, J. M.; Jain, P. K.; Ewers, T.; Alivisatos, A. P. Localized Surface Plasmon Resonances Arising from Free Carriers in Doped Quantum Dots. *Nat. Mater.* **2011**, *10*, 361–366.
39. Oshurko, V. B. Imaging Thermal Fields in Nonlinear Photoacoustics. *Tech. Phys. Lett.* **2006**, *32*, 691–693.

40. Egerev, S. V.; Oraevsky, A. A. Optothermoacoustic Phenomena in Highly Diluted Suspensions of Gold Nanoparticles. *Int. J. Thermophys.* **2008**, *29*, 2116–2125.
41. Sanchot, A.; Baffou, G.; Marty, R.; Arbouet, A.; Quidant, R.; Girard, C.; Dujardin, E. Plasmonic Nanoparticle Networks for Light and Heat Concentration. *ACS Nano* **2012**, *6*, 3434–3440.
42. Pazos-Perez, N.; Baranov, D.; Irsen, S.; Hilgendorff, M.; Liz-Marzan, L. M.; Giersig, M. Synthesis of Flexible, Ultrathin Gold Nanowires in Organic Media. *Langmuir* **2008**, *24*, 9855–9860.
43. Wijaya, A.; Schaffer, S. B.; Pallares, I. G.; Hamad-Schifferli, K. Selective Release of Multiple DNA Oligonucleotides from Gold Nanorods. *ACS Nano* **2009**, *3*, 80–86.
44. Li, N.; Yuan, R.; Chai, Y.; Chen, S.; An, H.; Li, W. New Antibody Immobilization Strategy Based on Gold Nanoparticles and Azure I/Multi-Walled Carbon Nanotube Composite Membranes for an Amperometric Enzyme Immunosensor. *J. Phys. Chem. C* **2007**, *111*, 8443–8450.
45. Song, K. H.; Wang, L. V. Deep Reflection-Mode Photoacoustic Imaging of Biological Tissue. *J. Biomed. Opt.* **2007**, *12*, 060503.
46. Zhang, T.; Cui, H. Z.; Fang, C. Y.; Su, L. J.; Ren, S. Q.; Chang, H. C.; Yang, X. M.; Forrest, M. L. Photoacoustic Contrast Imaging of Biological Tissues with Nanodiamonds Fabricated for High near-Infrared Absorbance. *J. Biomed. Opt.* **2013**, *18*, 026018.